ASME Journal of Vibration and Acoustics
Online journal at:
https://asmedigitalcollection.asme.org/vibrationacoustics

Random Wave Energy Conversion of a Spar–Floater System via the Inerter Pendulum Vibration Absorber Integration

Guoxin Li
Department of Mechanical Engineering,
Michigan State University,
East Lansing, MI 48824
e-mail: liguoxin@msu.edu

Wei-Che Tai[1]
Department of Mechanical Engineering,
Michigan State University,
East Lansing, MI 48824
e-mail: taiweich@msu.edu

Incorporating wave energy converters (WECs) into existing oceanographic instrument systems and offshore floating platforms can not only enhance the performance of these applications but reduce operational expenses. This article studies a system integrating a floater WEC with a floating spar platform via the inerter pendulum vibration absorber with a power take-off (IPVA-PTO) mechanism, with a focus on random wave excitation. Experiments and simulations performed on a simplified system in which the WEC is held fixed and radiation damping is absent reveal that the power spectral density (PSD) of the system consists of odd-order superharmonics when the peak frequency of wave excitation is equal to the natural frequency of the system. It is found that the odd-order superharmonics are created by the IPVA and have a strong correlation with an enhancement in power output. Simulations without the aforementioned simplifications confirm the odd-order superharmonics and the correlation, and demonstrate an improvement in the capture width ratio (CWR) of 161.4% at resonance without compromising the response amplitude operator (RAO) of the spar, in comparison with a linear benchmark with optimal electrical damping. [DOI: 10.1115/1.4067250]

Keywords: IPVA-PTO, random wave, energy, RAO, CWR, wave energy conversion, nonlinear vibration

1 Introduction

The rapid increase in global energy demand, coupled with the growing concerns over environmental pollution and climate change, has propelled the search for renewable and clean energy sources. Among these, ocean wave energy stands out due to its vast potential and relatively untapped status. Despite active efforts in ocean exploration, nearly 80% of the world's oceans remain untapped and unexplored. To facilitate further investigation, the development of new instruments, platforms, and tools is underway. The use of marine instrumentation, such as weather buoys, profiling instruments, and tsunami warning devices, is growing rapidly worldwide, driven by advancements in technology that allow for more comprehensive and cost-effective monitoring of the oceans [1].

One major limitation of oceanic instrument systems is their high energy demands. For example, ocean observation buoys can require anywhere from 10 to 600 kW of power, while many buoys used by the National Oceanic and Atmospheric Administration (NOAA) typically need between 40 and 200 W [1]. This considerable energy requirement underscores the potential of wave energy as a viable power source for these devices, particularly since it is often abundant in the areas where these systems are deployed. Take, for example, the Station 42055 Buoy operated by NOAA in the Gulf of Mexico, where the significant wave height averages around 3 ft and the average wave period is approximately 4.7 s[2]. According to the formula in Ref. [2], this average wave period will result in peak wave periods ranging between 4.44 and 6.91 s. Based on these parameters, the estimated wave power resource at this location is about 2 kW/m [1]. In this context, a wave energy converter (WEC) [3–6] deployed in the same area could sufficiently power oceanic instrument systems requiring between 40 and 200 W if its capture width ratio (CWR) is between 0.63% and 3.17%. This range is achievable with existing WECs that are compatible in size with oceanic instrument systems [7].

Furthermore, the oceans harbor extensive reserves of minerals and hydrocarbons, which can be extracted through methods such as passive adsorption and electrochemical processes. The extraction infrastructure, including platforms and equipment, also demands considerable electrical power for various operations: deploying and retrieving adsorbent films, pumping seawater, conducting electrochemical extractions (e.g., producing hydrogen and oxygen directly from seawater via electrolysis), and powering essential safety and monitoring systems. According to Ref. [8], achieving hydrogen production of 1 Nm^3 requires 4.2 kW of power.

[1]Corresponding author.

Contributed by the Technical Committee on Vibration and Sound of ASME for publication in the Journal of Vibration and Acoustics. Manuscript received July 8, 2024; final manuscript received November 7, 2024; published online December 12, 2024. Assoc. Editor: Mark Jankauski.

[2]https://www.ndbc.noaa.gov/

Theoretically, power generation of kilowatts or higher can be achieved by increasing the size of WECs, as the CWR improves with size [7]. However, the current cost of wave energy generation exceeds that of alternative renewable sources [9]. Enlarging WECs also leads to higher expenses related to installation, anchoring, and foundational support, as well as operational and maintenance activities, which account for approximately 40–50% of the total life cycle costs of wave energy projects [10]. This further complicates the cost-effectiveness of WECs.

A promising solution is to integrate WECs with the existing offshore floating platforms [10–15]. This approach offers significant advantages. First, the WECs can directly supply electricity to the platforms, which reduces or even eliminates the reliance on diesel generators or expensive, immobile shore-connected cables [16,17]. Second, by sharing infrastructure, equipment, mooring and anchoring systems, and monitoring methods [10], the overall cost of wave energy generation can be significantly lowered.

There are many examples of integrating WECs with the existing structures. A notable example is the spar–floater system [11–13], which consists of a long and slender spar that extends deep below the water surface to provide buoyancy and stability, and a coaxial annular floater that acts as a WEC. This study is based on this spar–floater system.

Despite the significant application potential and numerous advantages of integrating WECs with spar platforms, challenges persist in optimizing energy conversion efficiency and maintaining structural integrity, especially in systems equipped with linear power take-off (PTO) units. Based on the Ocean Data Gathering Program (ODGP) Spectrum Analysis Bands for the Gulf of Mexico [18], wave periods in the Gulf of Mexico corresponding to the center frequencies span a broad range, from approximately 0.74 to 49.64 s. Within this range, periods of 5–10 s are particularly typical [19,20]. However, the ODGP data also highlight the presence of long-period waves extending well beyond 10 s, which must be taken into account for the stability of offshore structures [21], especially when these periods approach the natural periods of the structures. As an illustration, spar platforms are designed with a heave natural period of 20–30 s [22,23] to avoid resonance with typical wave periods, thereby preventing potential damage.

However, conventional heaving WECs operate based on the principle of linear resonance, requiring their heave natural period to be close to the typical wave period to maximize energy collection efficiency. When integrating such WECs with spar platforms, the resonance characteristics can amplify the platform's heave motion [11,13], potentially leading to Mathieu instability [12]. This instability may exacerbate the fatigue of the mooring and riser systems, potentially resulting in system failure. Therefore, a fundamental conflict exists between optimizing wave energy conversion efficiency and maintaining hydrodynamic stability in such integrated systems.

Recent research on internal resonance has shown promise in achieving concurrent vibration mitigation and energy harvesting. Gupta and Tai [24–26] have investigated integration of an inerter pendulum vibration absorber (IPVA) with a two-body WEC system. The findings of their research indicate that incorporating the IPVA into the WEC system demonstrates simultaneous improvement on the efficiency of energy conversion and vibration suppression via 1:2 internal resonance. Nevertheless, their research predominantly explored scenarios under regular wave conditions without considering the influence of drag force and random wave excitation, which is insufficient to reflect realistic oceanic conditions.

This study extends the previous research by integrating drag damping and considering stochastic wave conditions to more accurately reflect marine environments. Specifically, the stochastic waves are generated based on the JOint North Sea WAve Project (JONSWAP) spectrum and harmonic random amplitude (HRA) method, providing a deeper understanding of the system's dynamics and capabilities in random wave environments, with particular attention to the dynamic response near the Spar's resonance frequency.

The remainder of this article is structured as follows: Sec. 2 introduces the system simulation. Following the generation of random waves, hydrodynamic coefficients are calculated based on the linear wave theory and the boundary element method, which are necessary for constructing the equation of motion (EOM) as highlighted by Ref. [27]. In Sec. 3, we verify the characteristics of random waves and demonstrate the effectiveness of simulations conducted using MATLAB. An experiment adapted for testing random wave excitation and the influence of drag damping are discussed in Sec. 4. Specifically, the experiment is built upon the previous work of Gupta and Tai [25,26], with modifications to the excitation force, i.e., changing it to a random wave force. The simulation results for random excitation are presented in Sec. 5. The study is concluded in Sec. 6.

2 Simulation of the System

As depicted in Fig. 1(*a*), the overall structure of the ocean wave energy conversion setup designed in this study is composed of a spar, a floater, and the IPVA-PTO system. The spar consists of two cylindrical sections, ensuring a relatively small structural mass while maintaining significant hydrostatic stiffness, thereby enhancing the device's stability and buoyancy in water. Adjacent to the spar, an annular floater operates in conjunction with the spar. Both entities, buoyantly positioned within the aquatic environment, are interconnected through the IPVA-PTO system.

According to Ref. [11], when the spar is integrated with the floater through a linear PTO, the floater significantly amplifies the spar's heave motion while only marginally influencing its pitch and surge. While it is necessary to consider the other five degrees-of-freedom (DOFs), i.e., surge, sway, roll, pitch, and yaw, to examine the overall performance, it is anticipated that most of the wave energy conversion will be contributed by heave motion. Therefore, this study focuses on heave motion and neglects the influence of the other DOFs. Additionally, frames similar to those used in Ref. [29] can be employed in wave tank experiments to restrict the spar and floater to heave motion only. In this way, mooring is not required; hence, it is disregarded in this study.

In the composition of the IPVA-PTO system, Fig. 1(*b*) elucidates the components, which include a ball screw with a lead (L) of 30 mm, a carrier, a generator, and a pendulum vibration absorber. This setup facilitates the conversion of the floater's vertical movements into mechanical energy, supported by a thrust bearing (not shown) that secures the screw to the spar within a structured housing. Consequently, the relative heaving displacement, denoted as $x_1 - x_2$, is converted into an angular displacement (θ), adhering to the relationship $x_1 - x_2 = R\theta$, where R represents the conversion ratio $L/2\pi$.

The carrier, firmly attached to the screw, has the same angular displacement (θ) and hosts a sun gear. The pendulum, modeled as a point mass for this analysis, oscillates about a pivot located a distance R_p from the center of the carrier. The dynamic interaction allows the mechanical motion to be converted into electrical energy by the generator's rotor, in conjunction with the screw and sun gear, with the instantaneous power represented by the formula $c_e(\dot{\theta} - \dot{\phi})^2$, where c_e represents the generator's electrical damping.

To be clear, the difference between the conventional two-body point absorber and the IPVA-PTO system is explained as follows. The former uses a mechanism, such as ball-screws or rack-pinions, to convert the relative heave motion into the rotation of a generator. In contrast, the IPVA-PTO system integrates a pendulum with the ball-screw mechanism. According to Ref. [25], the angular displacement of the pendulum can undergo a pitchfork bifurcation when its length exceeds a certain threshold. When this happens, the pendulum will exhibit two stable equilibria. By expanding the system around these equilibria using a Taylor series, Gupta and Tai [30] demonstrated that a period-doubling bifurcation in the

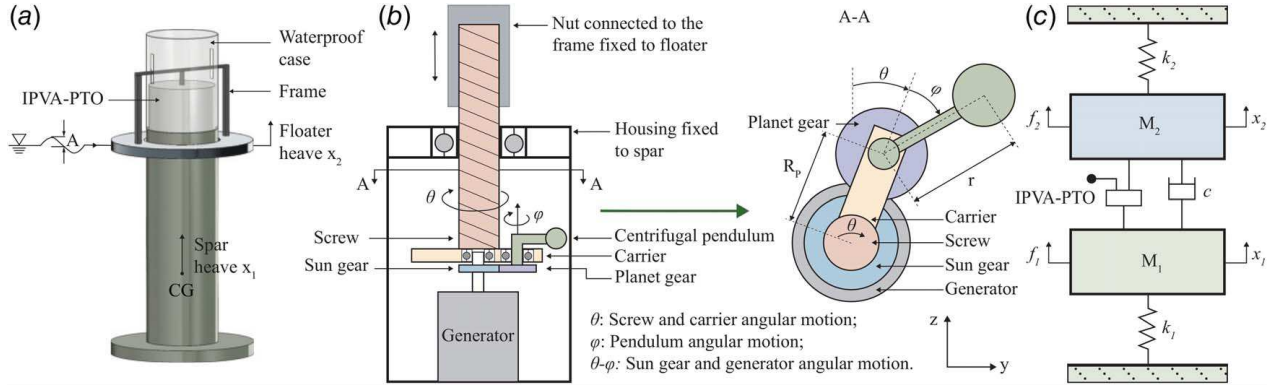

Fig. 1 The IPVA-PTO system integrated in a spar–floater setup for wave energy conversion: (*a*) energy conversion setup, (*b*) the IPVA-PTO system [28], and (*c*) mathematical model [28]

system's harmonic response leads to a 1:2 internal resonance, effectively transferring the vibration energy from the spar to the pendulum [25]. Subsequently, Gupta and Tai [26] showed that as the vibration energy of the spar was transferred to the pendulum, the spar's hydrodynamic response diminished, while the pendulum's vibrations intensified, thereby enhancing energy conversion efficiency as the generator was driven by the pendulum. As the previous studies only considered regular wave excitation, these insights inspire our investigation into the potential for internal resonance under irregular wave excitation.

To simulate the system's motion, the EOM for the system is derived. This requires initial determination of the drag force and the random wave force, which will be addressed in the subsequent two subsections, culminating in the formulation of the system's EOM.

2.1 System Scaling. The principle of similitude is essential for ensuring dynamic consistency between the full-scale prototype and the scaled model. Based on the Navier–Stokes equation, four primary scaling laws can be derived [31]: the Strouhal, Euler, Reynolds, and Froude scaling laws. In practice, it is generally not possible to satisfy all of these scaling laws simultaneously in experiments. For wave tank tests, where viscous effects are minimal, the Froude scaling law is typically used to control the dynamic characteristics of the scaled model [32]. However, this may alter other force ratios, such as viscous, surface tension, elastic, and pressure forces. For instance, Ref. [22] has shown that heave friction increases with an increase in the scaling ratio. Nonetheless, studies such as Refs. [29,33,34] demonstrate that these scaling effects are negligibly small; hence, the Froude scaling law is employed hereinafter. The scaling factors for various variables are presented in Table 1 [12,29].

A typical spar platform in the Gulf of Mexico, such as the Horn Mountain, has a diameter of 30 m [35]. Referring to the dimensions, optimal operating frequencies, and wave height ranges provided by the Marine Hydrodynamic Lab at the University of Michigan [36], the spar in this study is designed with an upper diameter of 0.3 m.

Table 1 Froude scaling of the variables

Variables	Scale factor	Value
Linear dimensions	λ	1 : 100
Velocity	$\lambda^{1/2}$	1 : 10
Acceleration	λ^{0}	1 : 1
Time or period	$\lambda^{1/2}$	1 : 10
Structure mass	λ^{3}	$1 : 10^6$
Volume	λ^{3}	$1 : 10^6$
Force	λ^{3}	$1 : 10^6$
Moment	λ^{4}	$1 : 10^8$
Power absorption	$\lambda^{7/2}$	$1 : 10^7$

Based on this, a scaling ratio of 1:100 is employed, and the dimensions for both the full-scale system and the scaled model are provided in Table 2.

2.2 Computation of Drag Damping. The drag force is modeled by the Morison equation [11], which takes the following form:

$$f_{\mathrm{d}} = -\frac{1}{2}\rho C_{\mathrm{d}} A \dot{x}|\dot{x}| \tag{1}$$

where

- $\dot{x}$ is the velocity of a linear combination of the DOFs. Specifically, in this study, as shown in Fig. 1, the relative motion between the heaving displacement x_1 of the spar and the heaving displacement x_2 of the floater, denoted by $x_1 - x_2$, is converted into the rotational angle θ of the screw by a ball-screw mechanism. The corresponding relationship is expressed as $x_1 - x_2 = R\theta$. To facilitate the derivation of the EOM, ψ is introduced to represent x_1 and x_2 as $x_1 = R(\theta + \psi)$ and $x_2 = R\psi$, respectively. Consequently, the velocities of the spar and the floater are given by $\dot{x}_1 = R(\dot{\theta} + \dot{\psi})$ and $\dot{x}_2 = R\dot{\psi}$, respectively.
- C_{d} is the drag coefficient, chosen according to the Det Norske Veritas (DNV) rules [37]. In this study, C_{d1} and C_{d2} are used to represent the drag coefficients of the spar and the floater, respectively. A is a projection area on the specific direction, associated with C_{d}.
- ρ is the density of seawater.

In this design, the formula can be finally elaborated as follows:

$$f_{\mathrm{d}} = \begin{bmatrix} -\frac{1}{2}\rho A_{\mathrm{spar}} C_{\mathrm{d1}} R^3 \left(\dot{\theta} + \dot{\psi}\right)\left|\dot{\theta} + \dot{\psi}\right| \\ -\frac{1}{2}\rho A_{\mathrm{spar}} C_{\mathrm{d1}} R^3 \left(\dot{\theta} + \dot{\psi}\right)\left|\dot{\theta} + \dot{\psi}\right| - \frac{1}{2}\rho A_{\mathrm{floater}} C_{\mathrm{d2}} R^3 \dot{\psi}|\dot{\psi}| \\ 0 \end{bmatrix} \tag{2}$$

Table 2 Dimensions of full-scale system and scaled model

Component	Scaled model (m)	Full scale (m)
Spar upper diameter	0.30	30
Spar lower diameter	0.60	60
Spar upper height	0.9	90
Spar lower height	0.05	5
Floater inner diameter	0.317	31.7
Floater outer diameter	0.595	59.5
Floater thickness	0.04	4

2.3 Random Wave Force. The modeling of wave behavior as a Gaussian process is a common approach in wave energy analysis, simplifying the statistical characterization of sea states for the assessment of WECs [19,38–40]. Therefore, this approach is employed in this work.

The statistical properties of Gaussian waves are completely characterized by their spectrum. The academic community has developed an extensive array of theoretical wave spectra, among which the JONSWAP spectrum stands out as a prominently utilized model in engineering research. The formulation proposed by Goda [2], as shown in Eq. (3), depends on the significant wave height H_s, the peak wave period T_p, and the peak-enhancement factor γ, which controls the sharpness of the spectral peak.

$$S_J(f) = \frac{\beta_J H_s^2}{T_p^4 f^5} \exp\left[-1.25\left(T_p \cdot f\right)^{-4}\right] \cdot \gamma^{\exp\left[-(T_p \cdot f-1)2/2\sigma^2\right]} \tag{3}$$

where

$$\begin{aligned} \beta_J &= \frac{0.0624 \cdot \left[1.094 - 0.01915 \ln(\gamma)\right]}{0.230 + 0.0336\gamma - 0.185\left(1.9 + \gamma\right)^{-1}}, \\ \sigma &= \begin{cases} \sigma_a = 0.07, f \le f_p \\ \sigma_b = 0.09, f > f_p \end{cases}, \\ \gamma &\in [1, 7] \end{aligned} \tag{4}$$

Various significant wave heights and peak wave periods used in the scaled model, along with their corresponding full-scale values, are provided in Table 3. This study pays particular attention to the dynamic response near the spar's heave natural frequency, which is why non-typical wave periods, such as 21.7 and 25 s (for the full-scale prototype) are listed. As for the selection of H_s, it was primarily based on the real sea conditions in Refs. [2,18,20,21,41,42] and the testing capabilities of the Marine Hydrodynamic Lab at the University of Michigan [36].

Harmonic superposition is a widely utilized method for generating random waves from a specified spectrum. To elaborate further, the HRA method, which chooses wave amplitudes randomly in harmonic superposition, is particularly notable for its extensive application in accurately representing the randomness of sea waves as observed in nature [43]. The formulation of HRA is written as follows:

$$y(t) = \sum_{k=1}^{M} A_k \cos\left(2\pi f_k t + \phi_k\right) \tag{5}$$

where $y(t)$ is considered as a univariate random process, which describes the free-surface wave elevation at a single location. The phase angle, represented by ϕ_k, is randomly chosen, following a uniform distribution in $[0, 2\pi]$. Additionally, A_k, which represents the wave amplitude, follows a Rayleigh distribution with a mean of zero and a variance of $2\nu_k$, namely,

$$\nu_k = \Delta f \cdot S_J(f_k) \tag{6}$$

where $\Delta f = f_c/M$, where f_c is the cut-off frequency and M denotes the total number of harmonics; see more detail in [38], $S_J(f_k)$ is the JONSWAP spectrum shown in Eq. (3), and $f_k = k\Delta f$ ($k \in [1, M]$) is the kth frequency.

It is challenging to address ocean wave input due to the intricate nature of ocean waves, which result from the superposition of numerous fundamental harmonics (in this study, involving the superposition of 1000 fundamental harmonics). This challenge primarily stems from the frequency-dependent nature of radiation force coefficients $\mathcal{R}$, as outlined in Eq. (13), rendering the traditional linear second-order differential equation inadequate for representing dynamics in the time domain. Cummins, as discussed in [44], introduced the application of integro-differential equation theory to model moving body's motion in arbitrary wave fields. This method builds upon the principles of the linear wave theory, expanding the concept of response superposition. Traditionally, this principle suggests that a system's response is the sum of its responses to individual sinusoidal inputs. This concept is further developed to propose the integration of cumulative responses of both the moving body and fluid to infinitesimal impulses [38].

The hydrodynamic impact on the spar and floater is segmented into three distinct forces according to the linear wave theory: the Froude–Krylov force, the diffraction force, and the radiation force. The Froude–Krylov force pertains to the unaltered incident wave field when the spar–floater system is absent. Conversely, the diffraction force emerges from alterations in the incident wave field owing to the presence of the spar–floater system. The radiation force is attributed to oscillations within this system, as explicated by Gupta et al. [25]. The Froude–Krylov and diffraction forces together give rise to the excitation force, while the radiation force gives rise to the added mass and radiation damping [19,38], which can be represented by the well-known Cummins' equation [44]:

$$F_{g,i} = -A_{\infty,i}\ddot{x}_i - \int_{\sigma=0}^{\infty} \kappa_{R,i}(\sigma)\dot{x}_i(t-\sigma)d\sigma + f_{ei}(t),\ i = 1, 2 \tag{7}$$

where f_{ei} is the excitation, due to the combined effects of the Froude–Krylov force and diffraction forces, and is calculated in Eq. (8).

$$f_{ei}(t) = \sum_{k=1}^{M} F_{ei}(f_k) A_k \cos\left(2\pi f_k t + \phi_k + \psi_k(f_k)\right) \tag{8}$$

where $F_{ei}(f_k)$ is the excitation force per wave amplitude at f_k under regular excitation, which is determined using ANSYS AQWA, A_k is the amplitude of wave component at f_k, same as A_k shown in Eq. (5), f_k is the frequency component, and ψ_k is the phase of excitation force $F_{ei}(f_k)$ at f_k under regular excitation, which is determined using ANSYS AQWA too.

In Eq. (7), $A_{\infty,i}$ and $\kappa_{R,i}(\sigma)$ are the added mass and radiation impulse response kernel, respectively. They are related to the radiation frequency-dependent damping and added mass $B_{R,i}(\Omega)$ and $A_{R,i}(\Omega)$, through Ogilvie's relations [45]:

$$\begin{aligned} B_{R,i}(\Omega) &= \int_{\sigma=0}^{\infty} \kappa_{R,i}(\sigma)\cos(\Omega\sigma)d\sigma,\ i = 1, 2 \\ A_{R,i}(\Omega) &= A_{\infty,i} - \frac{1}{\Omega}\int_{\sigma=0}^{\infty} \kappa_{R,i}(\sigma)\sin(\Omega\sigma)d\sigma,\ i = 1, 2 \end{aligned} \tag{9}$$

and

$$A_{\infty,i} = \lim_{\Omega\to\infty} A_{R,i}(\Omega) \tag{10}$$

The hydrodynamic coefficients $A_{R,i}(\Omega)$ and $B_{R,i}(\Omega)$ are determined utilizing ANSYS AQWA. Although $A_{R,i}(\Omega)$ and $B_{R,i}(\Omega)$ can be determined, the convolution term in Cummins' equation still presents a significant computational challenge within the framework

Table 3 Wave parameters for scaled model and full-scale prototype

Variables	Scaling ratio	Scaled model	Full scale
$H_s(m)$	1 : 100	0.008	0.8
		0.015	1.5
		0.025	2.5
$T_p(s)$	1 : 10	1	10
		1.25	12.5
		1.5	15
		2.17	21.7
		2.5	25

Note: Each H_s value applies to all T_p values in both the scaled model and the full-scale prototype.

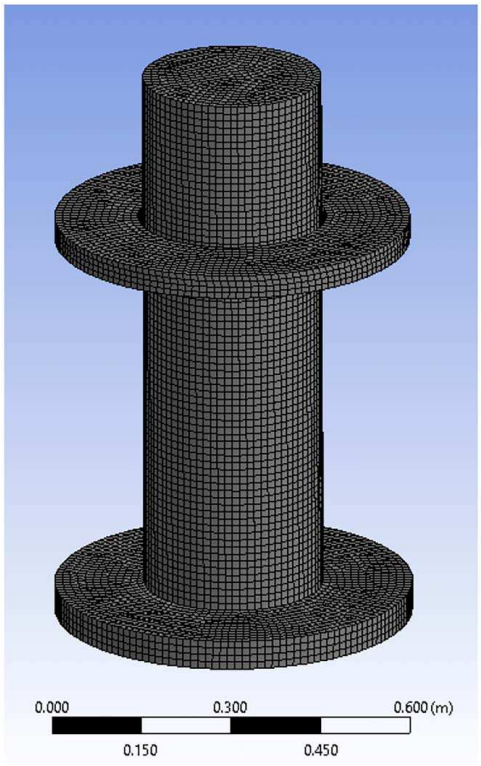

Fig. 2 Mesh of the spar and floater system

of time-marching numerical integration processes. The necessity of direct calculation of the convolution integral compels the use of numerical schemes that adhere to a fixed time-step for optimal efficiency.

Alternatively, to avoid the direct computation of the convolution integral, a commonly adopted strategy is the application of a state-space approximation. This method simplifies the representation of the radiation memory term, as delineated in the following equation:

$$\begin{aligned} \dot{y}_1^{SS} &= A_1^{SS} y_1^{SS} + B_1^{SS}(\dot{\theta} + \dot{\psi}) \\ r_1 &= C_1^{SS} y_1^{SS} + D_1^{SS}(\dot{\theta} + \dot{\psi}) \end{aligned} \tag{11}$$

$$\begin{aligned} \dot{y}_2^{SS} &= A_2^{SS} y_2^{SS} + B_2^{SS}\dot{\psi} \\ r_2 &= C_2^{SS} y_2^{SS} + D_2^{SS}\dot{\psi} \end{aligned} \tag{12}$$

where y_i^{SS} (i=1,2) is a nonphysical state vector of which the size depends on the order chosen for the state-space approximation, and A_i^{SS}, B_i^{SS}, C_i^{SS}, and D_i^{SS} are matrix, vectors, and scalar of appropriate dimensions, respectively. These can be calculated and then reduced in MATLAB using imp2ss and balmr functions [46,47]. Furthermore, θ and ψ represent the system's two DOFs, and r_1 and r_2 denote the approximations of the convolution integral.

Figure 2 illustrates the mesh configuration of the system as utilized in AQWA. The generated mesh information is as follows: total elements: 39,724; external surface diffracting elements: 28,184; and external surface nondiffracting elements: 11,540. Figures 3(*a*) and 3(*b*) depict, individually, the added mass, radiation damping, as well as the excitation force and phase angles for the spar and floater. Meanwhile, Fig. 4 presents the convolution kernels for the spar and floater.

Notably, significant peaks are observed at frequencies around 2.6 Hz. As demonstrated in Refs. [48,49], this phenomenon is likely attributed to the standing wave effect, which induces substantial changes in hydrodynamic forces, with radiation damping exhibiting delta function-like behavior and added mass showing pronounced maxima and negative minima, confined to a relatively narrow frequency band.

2.4 Equation of Motion. Figure 1(*c*) presents the equivalent mathematical model of the entire system. Utilizing Lagrange's equations as derived in Ref. [25], incorporating drag force and random wave force rather than regular wave force as the excitation force yields the equation of motion of the system. Subsequent to this derivation, the rescaling of the time variable and transformation of the resulting EOM into a dimensionless format is performed. This transformation aims to facilitate subsequent analysis, yielding the dimensionless form of the EOM, denoted as Eq. (13).

$$\mathbf{M}\mathbf{x}'' + \mathbf{C}\mathbf{x}' + \mathbf{K}\mathbf{x} + \mathcal{R}(\mathbf{x}') = \mathbf{f} + \mathbf{d} \tag{13}$$

where

$$\begin{aligned} \mathbf{M} &= \begin{bmatrix} a_{11} & a_{12} & a_{13} \\ a_{12} & a_{22} & 0 \\ a_{13} & 0 & a_{33} \end{bmatrix}, \mathbf{C} = \begin{bmatrix} \xi + \xi_e & 0 & -\xi_e \\ 0 & 0 & 0 \\ -\xi_e & 0 & \xi_e \end{bmatrix}, \\ \mathbf{K} &= \begin{bmatrix} 1 & 1 & 0 \\ 1 & 1 + \mu_F \omega_r^2 & 0 \\ 0 & 0 & 0 \end{bmatrix}, \mathcal{R}(\mathbf{x}') = \frac{1}{M_1 \omega_0^2} \begin{bmatrix} r_1 \\ r_1 + r_2 \\ 0 \end{bmatrix}, \\ \mathbf{f} &= \begin{bmatrix} f_{e,1} + 2\eta\mu_r \theta' \phi' \sin\phi + \eta\mu_r \phi'^2 \sin\phi \\ f_{e,1} + f_{e,2} \\ -\eta\mu_r \theta'^2 \sin\phi \end{bmatrix}, \mathbf{x} = \begin{bmatrix} \theta \\ \psi \\ \phi \end{bmatrix}, \\ \boldsymbol{d} &= \frac{R}{M_1} \begin{bmatrix} C_1(\theta' + \psi')|\theta' + \psi'| \\ C_1(\theta' + \psi')|\theta' + \psi'| + C_2\psi'|\psi'| \\ 0 \end{bmatrix} \end{aligned} \tag{14}$$

Here,

$$\begin{aligned} &a_{11} = 1 + (1 + \eta^2)\mu_r + \mu_{bsc} + \mu_p + 2\eta\mu_r \cos\phi + \mu_g + \mu_{A\infty,1}, \\ &a_{12} = 1 + \mu_{A\infty,1}, a_{13} = -\mu_g + \mu_p + \eta^2\mu_r + \eta\mu_r \cos\phi, \\ &a_{22} = 1 + \mu_F + \mu_{A\infty,1} + \mu_{A\infty,2}, a_{33} = \mu_p + \eta^2\mu_r + \mu_g, \\ &r_1 = \int_0^\infty \kappa_1\left(\frac{s}{\omega_0}\right)\left[\theta'(\tau - s) + \psi'(\tau - s)\right]ds, \\ &r_2 = \int_0^\infty \kappa_2\left(\frac{s}{\omega_0}\right)\psi'(\tau - s)ds, \\ &C_1 = -\frac{1}{2}\rho A_{spar} C_{d1}, C_2 = -\frac{1}{2}\rho A_{floater} C_{d2} \end{aligned} \tag{15}$$

and

$$\begin{aligned} &\eta_g = \frac{J_r}{M_1 R^2}, \mu_F = \frac{M_2}{M_1}, \eta = \frac{r}{R_p}, \omega_0 = \sqrt{\frac{k_1}{M_1}}, \omega_2 = \sqrt{\frac{k_2}{M_2}}, \\ &\mu_r = \frac{mR_p^2}{M_1 R^2}, \mu_{bsc} = \frac{J_{bsc}}{M_1 R^2}, \mu_p = \frac{J_p}{M_1 R^2}, \omega_r = \frac{\omega_2}{\omega_0}, \\ &\tau = \omega_0 t, \xi = \frac{c}{\omega_0 M_1}, \xi_e = \frac{c_e}{\omega_0 M_1 R^2}, ()' = \frac{d()}{d\tau}, \\ &f_{e,1} = \frac{f_{e1}}{\omega_0^2 M_1 R}, f_{e,2} = \frac{f_{e2}}{\omega_0^2 M_1 R}, \mu_{A\infty,1} = \frac{A_{\infty,1}}{M_1}, \mu_{A\infty,2} = \frac{A_{\infty,2}}{M_1} \end{aligned} \tag{16}$$

In Eq. (16), M_1 and M_2 are the masses corresponding to the spar and the floater, respectively. The terms k_1 and k_2 are associated with their hydrostatic stiffness. The mass ratio of M_1 over M_2 is expressed through μ_F. The natural frequency ratio of the floater and the spar is denoted as ω_r. Moreover, ξ denotes the system's mechanical damping ratio, whereas ξ_e refers to the electrical damping ratio. The ratio between the carrier length r and the pendulum length R_p is captured by the parameter η. Additionally, C_1 and C_2 quantify components of the drag force, correlating to the expression $-\frac{1}{2}\rho C_d A$. The normalized moments of inertia for the generator

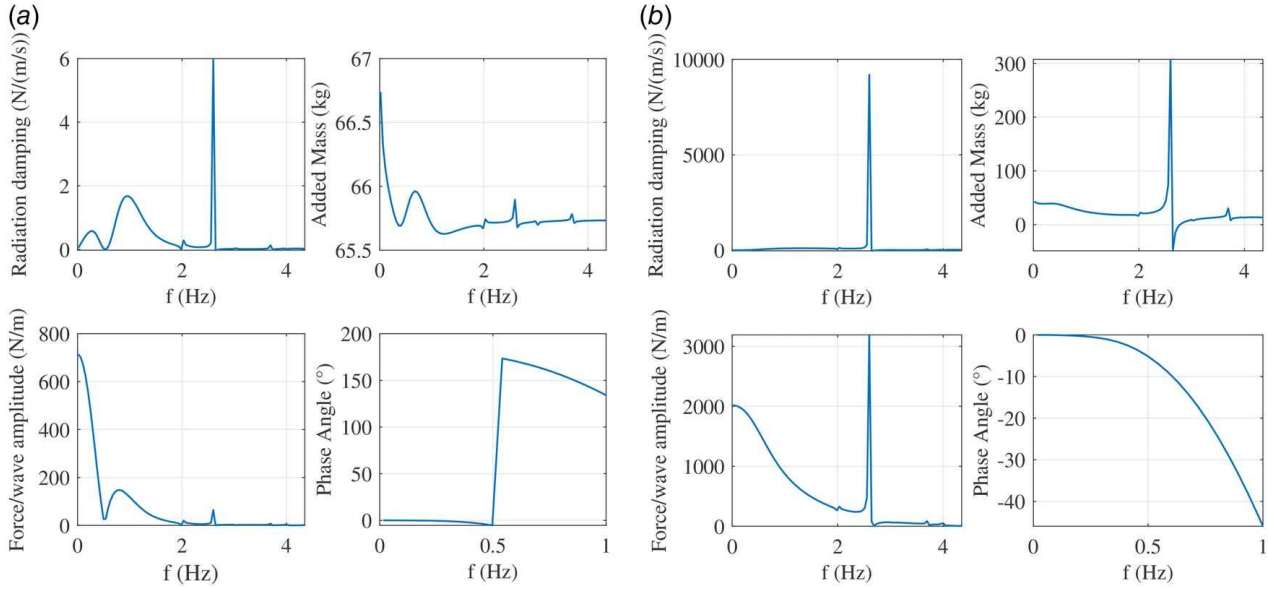

Fig. 3 Hydrodynamic data from AQWA: (*a*) spar and (*b*) floater

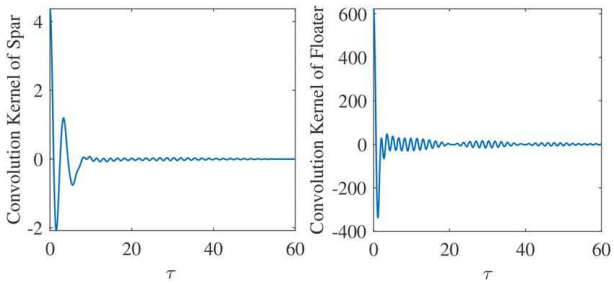

Fig. 4 Convolution kernels of spar and floater

rotor J_r, ball-screw-carrier assembly J_{bsc}, and pendulum J_p are represented by η_g, μ_{bsc}, and μ_r, respectively. Finally, the normalized added masses, which reflect the hydrodynamic effects on the system's inertial properties, are denoted by $\mu_{A\infty,1}$ and $\mu_{A\infty,2}$ for the spar and floater, respectively. All of them are nondimensional and do not have any units, except for M_1 and M_2 (kg), k_1 and k_2 (N/m), ω_0 and ω_2 (Hz), and R (m).

The geometric parameters of the spar and floater are listed in Table 2, while the PTO's parameters are identical to those of the experimental setup that will be discussed in Sec. 4. The materials for the spar and floater are chosen such that the first resonance frequency of the system is around 0.46 Hz, a suitable value for testing in a typical wave tank, such as the Marine Hydrodynamic Lab at the University of Michigan [36].

After finalizing the structural design and selecting the materials, the corresponding masses are inherently determined. Parameters such as hydrostatic stiffness and added mass are obtained from ANSYS AQWA. The system parameters are then nondimensionalized using Eq. (16). The physical and nondimensional parameters are listed in Table 4.

Upon deriving the EOM, this study utilizes the ODE45 function in MATLAB to compute the solutions, thereby simulating the system's behavior.

Table 4 Parameters in EOM

Parameter	Value	Parameter	Value	Parameter	Value
M_1	58.9700	C_1	0.4556	μ_r	0.6541
M_2	4.0100	C_2	0.8500	μ_p	0.0753
k_1	706.4049	ξ	0.3136	μ_{bsc}	0.4490
k_2	1996.6791	ξ_e	0.0700	$\mu_{A\infty,1}$	1.1147
ω_r	6.4477	η	0.4000	$\mu_{A\infty,2}$	0.2221
R	0.0048	η_g	0.0440		

3 Validation

Due to the high costs and stringent requirements associated with wave tank experiments, it is imperative to first validate simulation results through numerical methods. The selection of quantities for validation is crucial; This study opts for the root-mean-square (RMS) of the Spar's displacement, denoted as $|x|_{\text{rms}}$, for validation purposes. However, given the inherent strong nonlinearity of the system, along with the pronounced randomness of the ocean wave, validating the response of this nonlinear system under random wave excitation proves challenging. Therefore, we separately validate the random wave and the nonlinear system without drag damping.

3.1 Validation of JONSWAP Spectrum. For the validation of random waves, the power spectral density (PSD) is utilized as the metric for assessment. The average PSD obtained from 500 waves, randomly generated via the HRA method (5), is compared with the established JONSWAP spectral benchmark. The illustrative outcomes, presented in Fig. 5, show the original JONSWAP spectrum along with PSDs derived from the 500 random waves processed through periodogram and pwelch functions in MATLAB in the first subfigure. These comparative results exhibit robust alignment and coherence, substantiating the simulation's fidelity to the expected Rayleigh distribution with variance of $2\nu_k$.

Furthermore, the second subfigure in Fig. 5 depicts a time series of wave heights generated by a random ocean wave modeled with the JONSWAP spectrum, along with the aggregated wave height time series resulting from the superposition of the 500 random waves. The third subfigure presents the temporal wave height values derived from the 500 random waves, the "Order (n)" in the subfigure refers to the sequence of the samples. These illustrations confirm that the random waves adhere to a distribution with a mean value of zero, thereby corroborating the statistical behavior expected from the theoretical model.

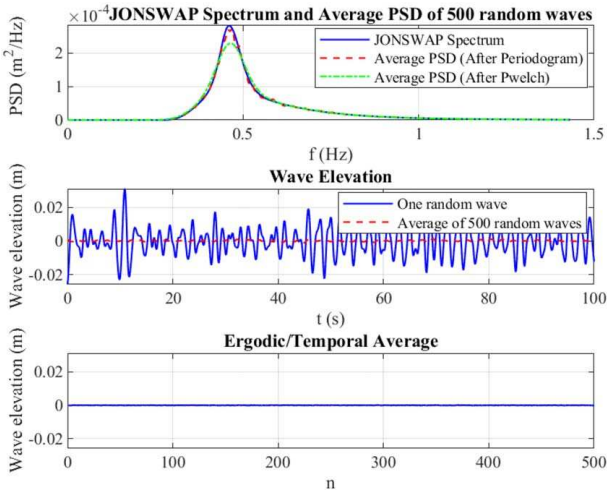

Fig. 5 Validation of random waves

3.2 Validation of Simulation in MATLAB. To validate the simulation of the system without drag damping under random wave excitation in MATLAB, the ODE45 solver is used to solve the EOM. This validation reflects a context where the system operates under linear forces in a linear manner. Specifically, the simulation is based on the underlying assumption that the pendulum of the IPVA-PTO system is locked at a fixed position. Subsequently, the RMS value of the spar displacement, x_{rms}, derived from the simulation, is computed using MATLAB's built-in rms function. This computed x_{rms} is then compared with the results obtained using the H2-norm method, as delineated in Eq. (17). This comparative analysis serves to validate the accuracy and reliability of the nonlinear system simulation.

$$|x|_{\text{rms}} = \left(\frac{1}{2\pi}\int_{-\infty}^{\infty} S_{\text{J}} \cdot |T(\omega)|^2 \cdot |H(\omega)|^2 d\omega\right)^{\frac{1}{2}} \tag{17}$$

where S_{J} is the JONSWAP spectrum, $H(\omega)$ is the excitation force per wave amplitude got from AQWA as shown in Fig. 3, and $T(\omega)$ is the frequency response function, which can be expressed with or without the state-space model as shown in Eq. (18):

$$T(\omega) = \frac{1}{-\omega^2(M + A_{\text{R}}(\omega)) - i\omega(C + B_{\text{R}}(\omega)) + K} \tag{18}$$

where M, C, and K are the matrices in Eq. (14), ω is the frequency of the excitation, and A_{R} and B_{R} represent added mass and radiation damping as shown in Eq. (9).

In Fig. 6(*a*), the simulation errors, benchmarked via the H2-norm, are depicted against the simulation time. Each mark represents the error of one simulated random wave (100 random waves in total). In addition, every random wave is the superposition of 100 harmonic waves, randomly generated via Eq. (5). Here, τ denotes the normalized simulation time, while $\Delta\tau$ and Num represent the normalized time-step size and their enumeration, respectively. Observations derived from the plot elucidate that the mean simulation discrepancy invariably sustains below a threshold of 8%. Furthermore, an elongation in simulation tenure results in a denser congregation of error points, thereby delineating an amelioration in simulation accuracy.

Figure 6(*b*) illustrates the relationship between the number of randomly generated harmonic waves aggregated to form a random wave and the simulation error, under the condition of sufficient simulation time. As demonstrated in the figure, the error gradually decreases with the increase in the number of randomly harmonic waves, generally stabilizing when the count reaches around 150.

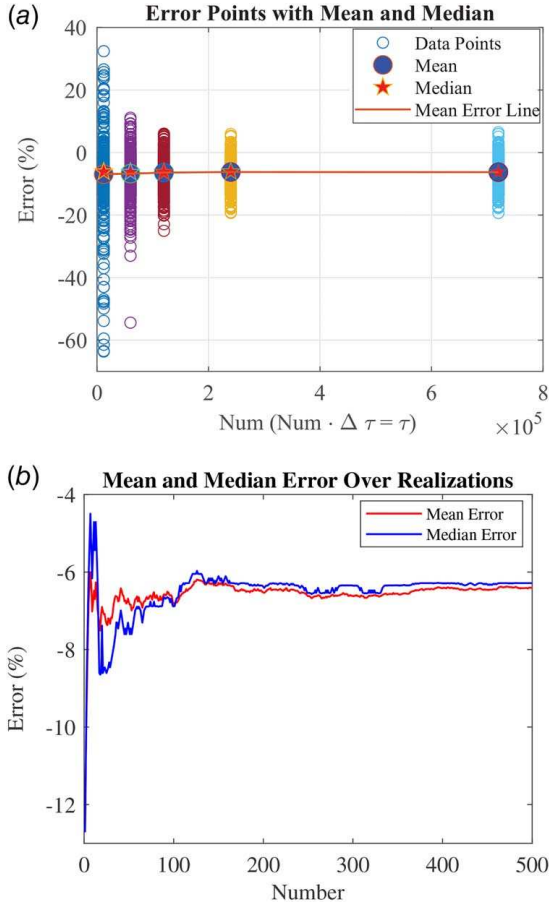

Fig. 6 Validation of simulation in MATLAB: (*a*) error points with mean and median and (*b*) mean and median error over realizations

4 Adapted Experiment and Drag Damping Analysis

Internal resonance is crucial for a class of nonlinear vibration absorbers [30,50], including the IPVA, to absorb vibration energy from the primary structures to which they are attached. In this section, experiments are performed on a simplified IPVA system to identify features of internal resonance when subjected to irregular wave excitation.

4.1 Adapted Experiment. Gupta and Tai [26] incorporated the IPVA-PTO into a single-degree-of-freedom structure subjected to harmonic excitation and experimentally validated the effects of a 1:2 internal resonance on energy conversion and response suppression. The experimental results demonstrated that the pendulum motion exhibited even-order subharmonics due to the internal resonance and found their correlation with energy transfer between the primary structure and the pendulum. However, their experiments were conducted under harmonic excitation, which does not accurately reflect the performance of the IPVA-PTO system under random ocean wave conditions.

Inspired by this, we examine the system's performance under random wave excitation, excluding drag and radiation damping, and focusing solely on the Froude–Krylov and diffraction forces, using the identical experimental setup. In comparison with harmonic excitation, this excitation more accurately reflects the randomness of real ocean wave conditions. The EOM for the setup was previously derived, followed by system identification and characterization. All the system parameters, such as mechanical damping and ball-screw-carrier inertia, were identified and listed in Ref. [26]. The experimental setup is shown in Fig. 7(*a*), with a

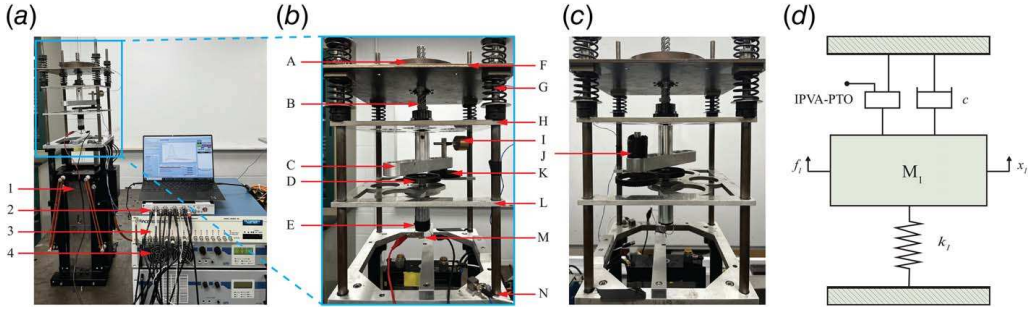

Fig. 7 Experimental design: (*a*) experimental setup, (*b*) IPVA-PTO design, (*c*) linear-PTO design, and (*d*) mathematical model. The labels indicate the following: 1: shaker, 2: spectrum analyzer and controller, 3: accelerometer signal conditioner, 4: shaker signal amplifier, A: primary mass, B: ball-screw system, C: carrier, D: sun gear, E: generator, F: top plate, G: connecting springs, H: ball-screw mounting plate, I: pendulum, J: payload, K: planetary gear, L: middle plate, M: load resistance, N: base plate.

close-up of the IPVA-PTO in Fig. 7(*b*). In addition, Fig. 7(*c*) shows a "linear-PTO" in which a payload (J) has been substituted for the pendulum. The payload is a hollow cylinder so that it accommodates the pendulum shaft in the center. As the center of mass of the payload is nearly at the center of rotation, it is modeled as a point mass with a negligible pendulum length.

The single-degree-of-freedom structure simulates a spar, analogous to the spar–floater system shown in Fig. 1(*a*), but with the floater fixed. Likewise, as illustrated in Fig. 7(*d*), the mathematical model of the experimental setup corresponds to that in Fig. 1(*c*) with the floater's mass M_2 fixed.

Notably, although the spar–floater system inherently has two DOFs, the significant disparities in the geometry, dimensions, and mass between the spar and floater introduce considerable differences in their dynamic behavior. Numerical simulations indicate that the first resonance frequency of the system is approximately 0.46 Hz, while the second resonance frequency is around 1.7 Hz, with a substantial gap between the two. At the first resonance frequency, the mode shape is dominated by the motion of the spar, whereas the floater's movement is negligible in comparison and can be approximated as quasi-static. Consequently, the system's dynamics near the first resonance can be approximated by a single-degree-of-freedom model. Given that this study primarily focuses on the system's response near the spar's heave natural frequency (first resonance), the floater is assumed to remain quasi-static. Thus, the experimental setup fits the scope of this research.

The JONSWAP spectrum with $H_s = 0.015$ m and $T_p = 1/0.46$ s is used to generate a random force on the spar. Specifically, this T_p value corresponds to the simulated first resonance frequency (0.46 Hz) of the system shown in Sec. 5. The PSD is divided by M_1^2 to obtain the PSD of the acceleration, where M_1 is the mass of the spar (see Table 4). The experimental setup will then be subjected to base excitation by a shaker (APS 113), whose acceleration has the same PSD. The RMS of the acceleration is about 8 m/s^2. Under this RMS value, the shaker (APS 113) has a limited bandwidth ranging from 2 Hz to 30 Hz. Therefore, the resonance frequency of the experimental setup is designed to be around 3.66 Hz, which is sufficiently above the lower limit of 2 Hz. The PSD's frequency is then scaled so that the peak wave frequency matches 3.66 Hz; see Fig. 8(*a*). Since the simulated first resonance frequency is 0.46 Hz, this design corresponds to a scale factor of $\lambda = 0.0158$, which would scale down the spar mass (58.97 kg) to just 0.2 g, which is an impractically low value. Hence, it is impossible to scale the mass according to the Froude scaling law due to hardware limitations. Instead, a mass of 3 kg is used in the experiment to generate noticeable nonlinear effects in the system.

Despite the discrepancy in mass, this experimental setup remains effective for investigating the system's response and energy harvesting capability when the system is near resonance.

The experimental setup operates as follows: First, the shaker, driven by a controller (Spider 80X) through an amplifier (APS 125), excites plates H, L, and N simultaneously. The excitation acceleration uses the same PSD described earlier. One accelerometer is attached to plate J to provide a closed-loop control for the shaker, while another accelerometer on top plate F monitors its motion. Both accelerometers are connected to an accelerometer signal conditioner (PCB 481) for signal processing. Eight springs maintain constant stiffness and allow relative motion between the primary mass system and the base plate system composed of plates H, L, and N. This relative linear motion is then converted into rotational motion by the ball-screw system, driving the oscillation of carrier C. The pendulum, mounted on but not fixed to the carrier, experiences vibration or rotation as a result. Consequently, the planetary and sun gears are driven, which subsequently rotate the generator rotor, converting mechanical energy into electrical

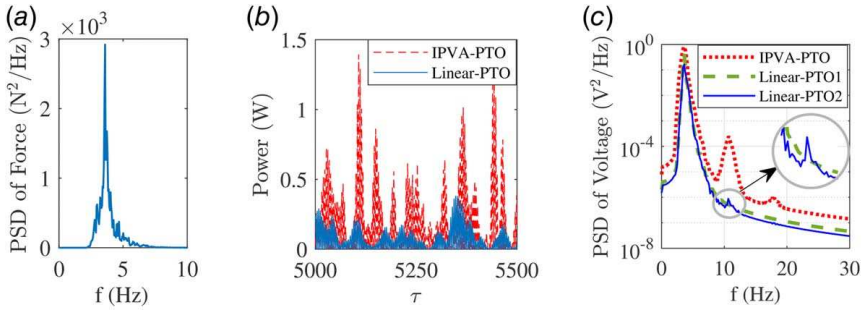

Fig. 8 (*a*) PSD of Force, (*b*) instantaneous power, with mean values of 0.3077 W for IPVA-PTO and 0.0924 W for linear-PTO from simulation, and (c) PSD of voltage from simulation. The dotted line represents the IPVA-PTO system, while the dashed line (linear-PTO1) corresponds to the linear-PTO system without drag damping, and the solid line (linear-PTO2) reflects the linear-PTO system with drag damping.

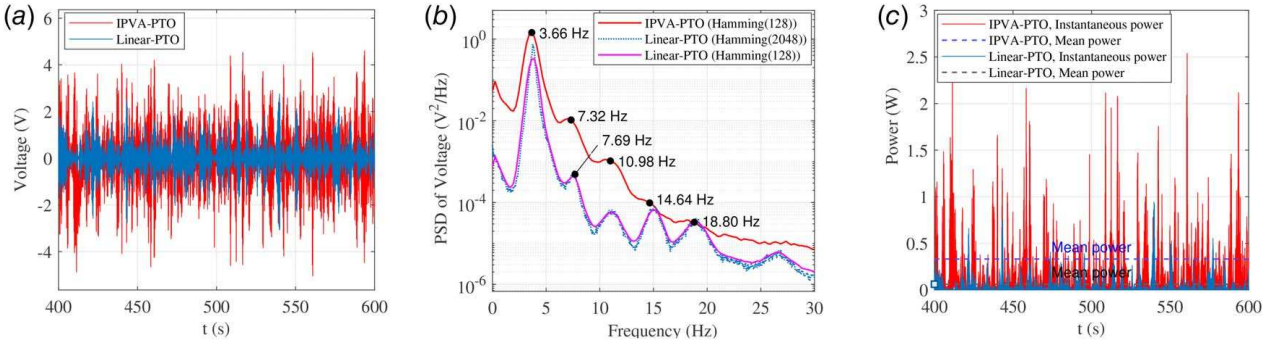

Fig. 9 Experiment results: (*a*) instantaneous voltage, (*b*) PSD of voltage, and (*c*) instantaneous power, with mean values of 0.33195 W for IPVA-PTO and 0.06186 W for linear-PTO

energy. Finally, the voltage at the generator terminals is measured using a spectrum analyzer (Spider 80X).

We perform simulations of the system's motion using MATLAB, with the parameter values previously identified through experiments in Ref. [26]. In these simulations, θ represents the angular displacement of the carrier, while ϕ denotes the angular displacement of the pendulum relative to the carrier. The instantaneous power, represented by $c_e(\dot{\theta}-\dot{\phi})^2$ and illustrated in Fig. 8(*b*), quantifies the harvested energy. The PSD of voltage, depicted in Fig. 8(*c*), highlights the energy distribution in the frequency domain. Specifically, the dashed line represents the performance of the linear-PTO system without drag damping, while the solid line includes its effect. The impact of drag damping will be analyzed in detail in Sec. 4.2. As illustrated in Fig. 8(*a*), the excitation force ranges between 0 and 10 Hz with a peak frequency of 3.66 Hz, matching the natural frequency of the experimental setup. Consequently, the results in Fig. 8(*c*) reveal a prominent peak at approximately 3.66 Hz. Additionally, we observe peaks at around 10.98 Hz and 18.3 Hz, which correspond to threefold and fivefold the fundamental frequency of 3.66 Hz, respectively. Although there are discrepancies in the mean power, the observed trends remain consistent.

To further verify our findings, we conduct experiments and compare the results with the simulation results. The experimental results are depicted in Fig. 9, with Fig. 9(*a*) showing the instantaneous voltage measurements. The PSD of the voltage, computed using MATLAB's pwelch function, is displayed in Fig. 9(*b*). This figure contrasts the results obtained using different window lengths in the pwelch function, specifically a Hamming window with lengths of 2048 and 128, to illustrate their impact on the PSD. Notably, in the linear-PTO system, when the window length is set to 128, the curve at the primary frequency bin exhibits a reduction in the peak value. This occurs because as the window length decreases, the curve becomes smoother, which may result in less prominent or sharp peaks. Figure 9(*c*) presents the corresponding harvested power and its mean value. A comparison between the simulation results and experimental data reveals a strong correlation, qualitatively confirming the presence of odd-order harmonics, which are not present in the linear-PTO system, and their association with higher power output in the IPVA-PTO system compared to the linear-PTO system.

In both the simulation and experimental results, for a fair comparison, the optimal[3] system with a linear PTO[4] is used as a benchmark, achieved by locking the pendulum of the IPVA-PTO system at a position such that the maximum value of the PSD of the linear system's voltage occurs around the same frequency as that of the IPVA-PTO system. From Fig. 9, we can observe that under the same excitation force, the energy harvested by the IPVA-PTO system is significantly greater than that by the linear-PTO, with the mean power being more than fivefold compared with the linear-PTO. By analyzing the PSD of the voltage, as shown in Fig. 9(*b*), we observe that the PSD of the voltage corresponding to the IPVA-PTO system exhibits distinct odd-order superharmonics under the same excitation conditions as the simulation. These superharmonics are also present in the linear-PTO system, but the corresponding PSD values are much smaller for the linear-PTO. This may be due to the payload having a small eccentricity, causing it to act as a pendulum with a very small pendulum length, resulting in similar but much weaker superharmonics. Additionally, we also observe a second-order (around 7.32 HZ) and fourth-order superharmonic (around 14.65 Hz) in both systems. The cause is still unknown. A hypothesis is that both systems may possess another vibration motion in this frequency range, e.g., the precession of carrier C. This hypothesis requires further investigation to be confirmed.

The study in Ref. [26] shows that internal resonance is manifested by secondary harmonics in the pendulum response. This leads us to the hypothesis that the odd-order superharmonics observed in our study are also a result of internal resonance. However, validating this hypothesis requires in-depth theoretical analysis, which is beyond the scope of the current work.

4.2 Fourier Coefficients of Drag Damping. To clearly investigate the impact of drag damping on the system response, we employ the harmonic balance method (HBM) [51] to study its behavior under regular wave excitation. Consequently, we first need to obtain the Fourier coefficients of drag damping. The drag force is defined in Eq. (1). For convenience, in subsequent expressions, we simplify the constant term as C_D, which is represented as follows:

$$f_d(t) = C_D \dot{x}|\dot{x}| \tag{19}$$

Let us assume $x = A\cos(\omega t) + B\sin(\omega t)$ and set $\phi = \omega t$. Then $\dot{x} = -\omega A\sin(\omega t) + \omega B\cos(\omega t)$. Performing a Fourier expansion of the expression yields

$$F_d(\phi) \cong a_0 + \sum_{n=1}^{\infty}\left[a_n\cos(n\phi) + b_n\sin(n\phi)\right] \tag{20}$$

where

$$a_n = \frac{2}{T}\int_0^T F_d\cos(n\omega t)\,dt,\ b_n = \frac{2}{T}\int_0^T F_d\sin(n\omega t)\,dt \tag{21}$$

[3]"Optimal" specifically refers to the configuration in which electrical damping within the linear system is optimized, under the constraint of ensuring practical applicability, to achieve the highest level of power conversion efficiency.

[4]When the pendulum is locked, the system becomes linear. However, in simulations, due to the nonlinear nature of drag damping, the system response remains nonlinear. For convenience in comparison, we still refer to it as "linear" in Fig. 8. In experiments, due to technical limitations, it is not feasible to lock the pendulum at a fixed angle. Here, placing a payload on the pendulum's rotation axis after removing the pendulum is used to create the linear system.

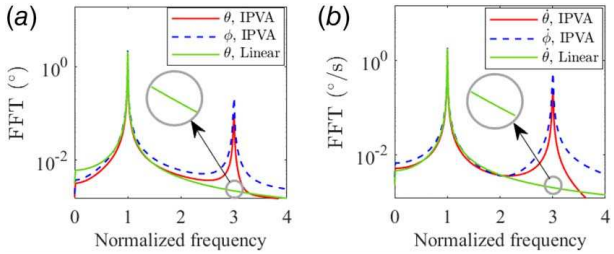

Fig. 10 FFT of response without drag damping: (*a*) angular displacement and (*b*) angular velocity

After straightforward integration, one finds

$$a_n = \begin{cases} \frac{8Ci^{n+1}\cos(n\phi)}{n(n^2-4)}, \ i=\sqrt{-1}, & \text{if } n=1,3,5,\ldots \\ 0, & \text{if } n=0,2,4,6,\ldots \end{cases} \tag{22}$$

and

$$b_n = \begin{cases} \frac{4C\left(-i^{n+1}+\sin\left(\frac{n\pi}{2}\right)\right)\sin(n\pi)}{n(n^2-4)\pi}, \ i=\sqrt{-1}, & \text{if } n=1,3,5,\ldots \\ 0, & \text{if } n=2,4,6,\ldots \end{cases} \tag{23}$$

where $C = \frac{C_D\omega^2}{\pi}\left(A^2+B^2\right)$.

Finally, the system response under regular wave excitation, obtained through HBM and validated using ODE45, is analyzed using the fast Fourier transform (FFT). These analyses, which highlight the response behavior with and without drag damping, are depicted in Figs. 10 and 11. Specifically, by comparing these figures, the emergence of a peak at a frequency that is three times the excitation frequency, which was not identified in earlier studies, can be attributed to the influence of drag force.

5 Simulation Investigation

Two measures are considered to assess the complete system's performance characteristics: the response amplitude operator (RAO) of the spar and the harvested energy normalized by the time scale, for which the calculation formulas are as follows:

$$\text{RAO} = \frac{|x_1|_{\text{rms}}}{H_s} \tag{24}$$

$$E = \int_{\tau_1}^{\tau_2} c_e\left(\dot{\theta}-\dot{\phi}\right)^2 d\tau \tag{25}$$

Additionally, to provide a clear comparison of the energy conversion efficiencies between the IPVA-PTO and linear-PTO systems under the same H_s conditions, the CWR is employed, which is

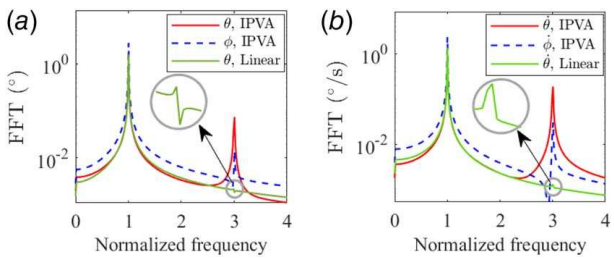

Fig. 11 FFT of response with drag damping: (*a*) angular displacement and (*b*) angular velocity

defined as the ratio between the capture width (CW) and the characteristic width of the WEC (B); that is, the ratio of absorbed wave power P_o (in kW) to the wave resource P_w (in kW/m) [2,52], divided by B [7,53,54]:

$$\text{CWR} = \frac{\text{CW}}{B} = \frac{P_o}{P_w B} \tag{26}$$

where

$$P_w = \frac{\rho g^2 H_s \alpha T_p}{64\pi} \tag{27}$$

with P_o being the mean of instantaneous absorbed power and B being the outer diameter of the floater [11,15]. The calibration coefficient (α) is generally estimated by assuming standard shapes of the wave energy spectrum. It is set to $\alpha = 0.9$ for a standard JONSWAP spectrum with a peak enhancement $\gamma = 3.3$ [55].

Since the ocean wave is random, the system response is also random; therefore, we use the average of 100 realizations for evaluation. The RAO is delineated as the RMS of the heave amplitude of the spar relative to the significant wave height, which represents one of the triad principal parameters within the JONSWAP spectrum. On the other hand, the normalized harvested energy is delineated as the quantity of energy flowing into the electrical domain within a normalized time duration.

As illustrated in Fig. 12, a comparative analysis elucidates the variations in energy capture and RAO of the spar under different significant wave heights H_s and peak wave periods T_p between the IPVA-PTO system and the optimal system with linear-PTO, which, as mentioned earlier, is used as a benchmark for a fair comparison.

Figure 12(*a*) demonstrates that as H_s increases, the harvested energy also increases, with the IPVA system consistently capturing more energy than the linear system. Additionally, two distinct peaks can be observed in the figure. The first peak occurs when the "peak wave frequency," which equals the reciprocal of the peak wave period, is approximately 0.24 Hz, roughly half of the system's first natural frequency. The second peak occurs at when the "peak wave frequency" is approximately 0.46 Hz, which is in close proximity to the system's first natural frequency.

As shown in Fig. 12(*b*), the capture width ratio of the IPVA-PTO exceeds that of the linear-PTO by more than 2.5 times when $H_s = 0.008$ m and $1/T_p = 0.46$ Hz. Similarly, a peak can be observed in Fig. 12(*c*) around 0.46 Hz. However, no significant peaks are observed around $1/T_p = 0.24$ Hz. Additionally, under the same H_s and T_p conditions, the RAO for the IPVA-PTO shows no substantial differences compared to the linear-PTO, with the IPVA-PTO being only slightly higher.

To evaluate the occurrence of resonance phenomena similar to those identified through FFT analysis under regular wave excitation, as demonstrated in Ref. [26], we analyzed the power spectrum density (PSD) of $\dot{\theta}$, PSD of $\dot{\theta}-\dot{\phi}$ (which corresponds to the harvested energy, noting that $\dot{\phi}=0$ in the linear-PTO system since the pendulum is locked), and PSD of $\theta+\phi$ (corresponding to the RAO of the spar). The results are illustrated in Figs. 13 and 14. When $H_s = 0.008$ m and $1/T_p = 0.46$ Hz, the IPVA-PTO system exhibits prominent odd-order primary and superharmonic components, where the frequencies at these peaks correspond to one, three, five, and seven times the peak wave frequency, a phenomenon not observed in the linear-PTO system. For a clear comparison, the influence of drag damping on superharmonics has been excluded. Furthermore, the PSD of $\dot{\theta}-\dot{\phi}$ in the IPVA-PTO system is significantly greater than that in the linear-PTO system, while the PSD of $\dot{\theta}+\dot{\phi}$ is only slightly higher in the IPVA-PTO system. This observation aligns well with the phenomena depicted in Fig. 12.

When $H_s = 0.008$ m and $1/T_p = 0.24$ Hz, in addition to the aforementioned odd-order superharmonics corresponding to the peak wave frequency of 0.24 Hz, we also observed a second-order superharmonic at 0.46 Hz, which corresponds to the system's first natural

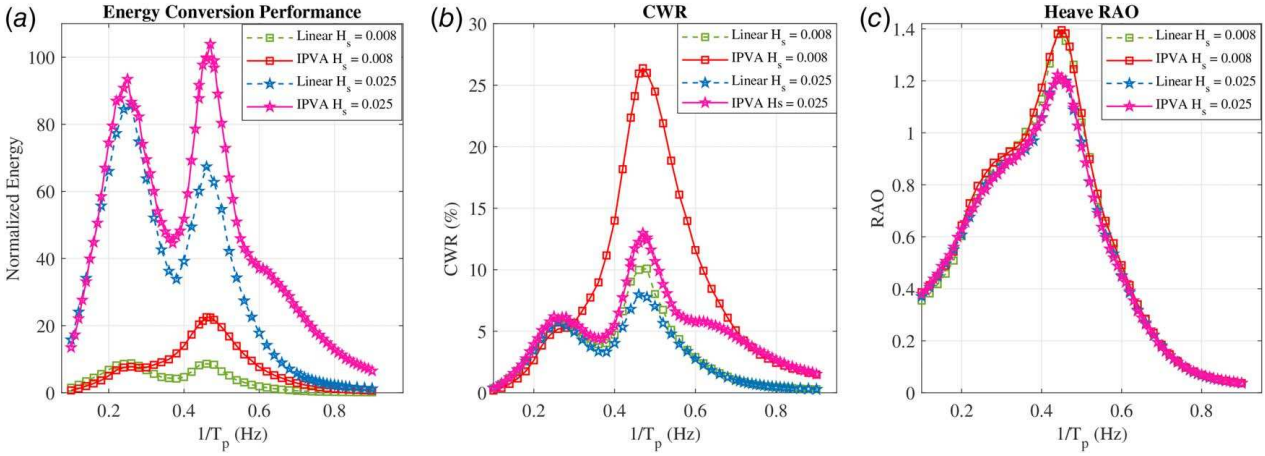

Fig. 12 Comparison of energy, CWR, and RAO with various H_s and T_p: (*a*) energy, (*b*) CWR, and (*c*) RAO

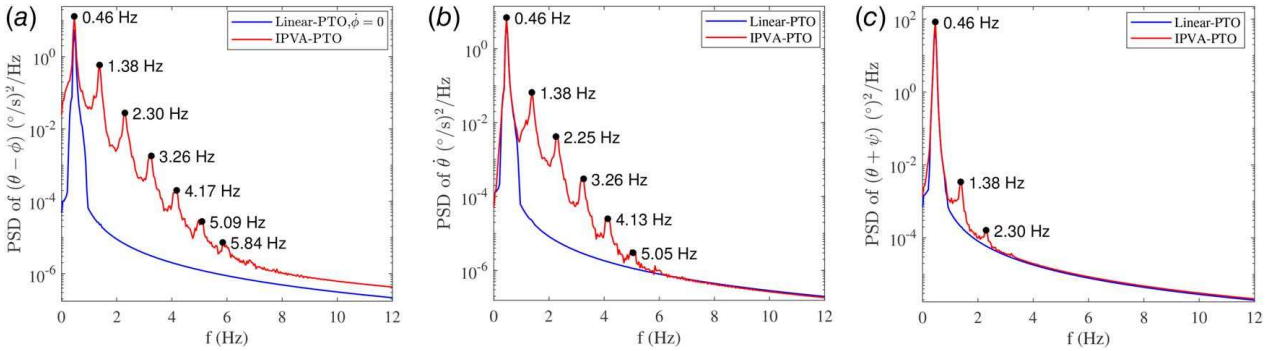

Fig. 13 PSD results for $H_s = 0.008$ and $T_p = 1/0.46$: (*a*) PSD of $(\dot{\theta}-\dot{\phi})$, (*b*) PSD of $\dot{\theta}$, and (*c*) PSD of $(\theta+\phi)$

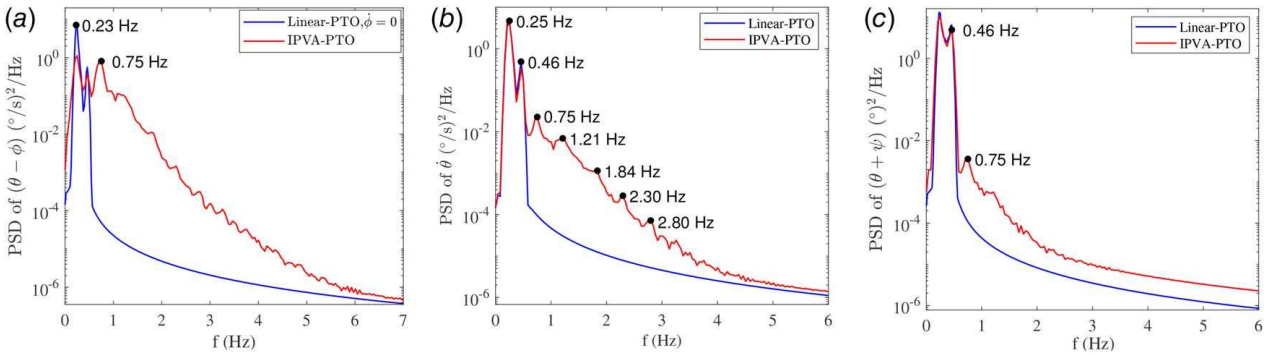

Fig. 14 PSD results for $H_s = 0.008$ and $T_p = 1/0.24$: (*a*) PSD of $(\dot{\theta}-\dot{\phi})$, (*b*) PSD of $\dot{\theta}$, and (*c*) PSD of $(\theta+\phi)$

frequency. We hypothesize that the odd-order and the second-order superharmonics observed in our study are resulted from internal resonance. However, validating this hypothesis is beyond the scope of the current work, and we will aim to address this in our future research.

In summary, Fig. 12 reveals that the energy harvested by the IPVA-PTO system is significantly higher than that of the linear system, while the RAO of the spar remains essentially identical between the optimal system with linear-PTO and the IPVA-PTO system. At $H_s = 0.008$ m and $1/T_p = 0.46$ Hz, which corresponds to the heave natural frequency of the spar, the harvested power is 0.98 W. According to the Froude scaling law, this scales up to 273.92 W when the floater's outer diameter is 3 m, the same as that of the Station 42055 Buoy, and 9.84 MW for the full-scale prototype. For typical wave periods ranging from 5 to 10 s, corresponding to scaled periods of 0.5–1 s in this study—where the floater's heave natural period lies—the energy conversion performance is dominated by the floater's dynamic response. However, a detailed analysis for this frequency range is reserved for a future study. Additionally, Figs. 13 and 14 present the simulated PSD results, which are similar to the experimental PSD of voltage results shown in Fig. 9(*b*). Moreover, the PSD of $\dot{\theta}-\dot{\phi}$ in the IPVA-PTO system is significantly greater than that in the linear-PTO system, while the PSD of $\dot{\theta}+\dot{\phi}$ is only slightly higher in the IPVA-PTO system, indicating that the two sets of results are in good agreement, further validating the findings.

6 Conclusion

This research demonstrates the effectiveness of the IPVA-integrated spar–floater–WEC system subjected to irregular wave excitation. The simulations and experiments with the IPVA-integrated single-degree-of-freedom system show that the PSD of the system consists of odd-order superharmonics when subjected to irregular wave excitation with the peak frequency equal to the natural frequency of the system. It is found that the odd-order superharmonics are created by the IPVA and have a strong correlation with the enhancement in power output. Also, the effect of drag damping is investigated in simulations with regular and random wave excitation. It is found that drag damping introduces odd-order superharmonics in the system response, appearing in the FFT under regular wave excitation and in the power spectrum density under random wave excitation. The simulations with the IPVA-integrated spar–floater–WEC system confirm the occurrence of the odd-order superharmonics and the correlation with the high power output when the peak frequency of the wave is equal to the first natural frequency of the system. In addition, when the peak wave frequency is nearly half the first natural frequency, the simulations also reveal a second-order superharmonic near the first natural frequency. In comparison with the linear benchmark with optimal electrical damping, the simulations demonstrate an improvement in the CWR of 161.4% at resonance without compromising the RAO of the spar.

Acknowledgment

This material is based upon work supported by the National Science Foundation. Any opinions, findings, and conclusions or recommendations expressed in this material are those of the authors and do not necessarily reflect the views of the National Science Foundation. Additionally, the authors are very much grateful to Ms. AnnaMaria Schneider for conducting experiments and collecting the data as well as the Marine Hydrodynamics Laboratory at the University of Michigan for their guidance on wave tank testing.

Funding Data

- National Science Foundation (Grant No. 2127495).

Conflict of Interest

There are no conflicts of interest.

Data Availability Statement

The datasets generated and supporting the findings of this article are obtainable from the corresponding author upon reasonable request.

References

[1] LiVecchi, A., Copping, A., Jenne, D., Gorton, A., Preus, R., Gill, G., Robichaud, R., Green, R., Geerlofs, S., Gore, S. et al., 2019, "Powering the Blue Economy; Exploring Opportunities for Marine Renewable Energy in Maritime Markets," US Department of Energy, Office of Energy Efficiency and Renewable Energy, WA, DC, 207.

[2] Goda, Y., 2010, *Random Seas and Design of Maritime Structures*, Vol. 33, World Scientific, Singapore.

[3] Palha, A., Mendes, L., Fortes, C. J., Brito-Melo, A., and Sarmento, A., 2010, "The Impact of Wave Energy Farms in the Shoreline Wave Climate: Portuguese Pilot Zone Case Study Using Pelamis Energy Wave Devices," Renew. Energy, **35**(1), pp. 62–77.

[4] Previsic, M., 2004, "Offshore Wave Energy Conversion Devices," Electric Power Research Institute (EPRI) Inc., Palo Alto, CA, pp. 26–130.

[5] Kofoed, J. P., Frigaard, P., Friis-Madsen, E., and Sørensen, H. C., 2006, "Prototype Testing of the Wave Energy Converter Wave Dragon," Renew. Energy, **31**(2), pp. 181–189.

[6] Babarit, A., Guglielmi, M., and Clément, A. H., 2009, "Declutching Control of a Wave Energy Converter," Ocean Eng., **36**(12–13), pp. 1015–1024.

[7] Babarit, A., 2015, "A Database of Capture Width Ratio of Wave Energy Converters," Renew. Energy, **80**, pp. 610–628.

[8] Saenz-Aguirre, A., Saenz, J., Ulazia, A., and Ibarra-Berastegui, G., 2022, "Optimal Strategies of Deployment of Far Offshore Co-located Wind-Wave Energy Farms," Energy Convers. Manage., **251**, p. 114914.

[9] Astariz, S., and Iglesias, G., 2015, "The Economics of Wave Energy: A Review," Renew. Sust. Energ. Rev., **45**, pp. 397–408.

[10] Nguyen, H. P., Wang, C., Tay, Z., and Luong, V., 2020, "Wave Energy Converter and Large Floating Platform Integration: A Review," Ocean Eng., **213**, p. 107768.

[11] Muliawan, M. J., Karimirad, M., and Moan, T., 2013, "Dynamic Response and Power Performance of a Combined Spar-Type Floating Wind Turbine and Coaxial Floating Wave Energy Converter," Renew. Energy, **50**, pp. 47–57.

[12] Wan, L., Gao, Z., and Moan, T., 2015, "Experimental and Numerical Study of Hydrodynamic Responses of a Combined Wind and Wave Energy Converter Concept in Survival Modes," Coast. Eng., **104**, pp. 151–169.

[13] Cheng, Z., Wen, T. R., Ong, M. C., and Wang, K., 2019, "Power Performance and Dynamic Responses of a Combined Floating Vertical Axis Wind Turbine and Wave Energy Converter Concept," Energy, **171**, pp. 190–204.

[14] Zhou, Y., Ning, D., Chen, L., Mayon, R., and Zhang, C., 2023, "Experimental Investigation on an OWC Wave Energy Converter Integrated Into a Floating Offshore Wind Turbine," Energy Convers. Manage., **276**, p. 116546.

[15] Michailides, C., 2021, "Hydrodynamic Response and Produced Power of a Combined Structure Consisting of a Spar and Heaving Type Wave Energy Converters," Energies, **14**(1), p. 225.

[16] Haces-Fernandez, F., Li, H., and Ramirez, D., 2018, "Assessment of the Potential of Energy Extracted From Waves and Wind to Supply Offshore Oil Platforms Operating in the Gulf of Mexico," Energies, **11**(5), p. 1084.

[17] Oliveira-Pinto, S., Rosa-Santos, P., and Taveira-Pinto, F., 2019, "Electricity Supply to Offshore Oil and Gas Platforms From Renewable Ocean Wave Energy: Overview and Case Study Analysis," Energy Convers. Manage., **186**, pp. 556–569.

[18] Forristall, G. Z., 1981, "Measurements of a Saturated Range in Ocean Wave Spectra," J. Geophys. Res. Oceans, **86**(C9), pp. 8075–8084.

[19] Liang, C., 2016, "On the Dynamics and Design of a Wave Energy Converter With Mechanical Motion Rectifier," Ph.D. thesis, State University of New York at Stony Brook, Stony Brook, NY.

[20] Hwang, P. A., Teague, W. J., Jacobs, G. A., and Wang, D. W., 1998, "A Statistical Comparison of Wind Speed, Wave Height, and Wave Period Derived From Satellite Altimeters and Ocean Buoys in the Gulf of Mexico Region," J. Geophys. Res. Oceans, **103**(C5), pp. 10451–10468.

[21] Amores, A., and Marcos, M., 2020, "Ocean Swells Along the Global Coastlines and Their Climate Projections for the Twenty-First Century," J. Clim., **33**(1), pp. 185–199.

[22] Subbulakshmi, A., and Sundaravadivelu, R., 2016, "Heave Damping of Spar Platform for Offshore Wind Turbine With Heave Plate," Ocean Eng., **121**, pp. 24–36.

[23] Koo, B., Kim, M., and Randall, R., 2004, "Mathieu Instability of a Spar Platform With Mooring and Risers," Ocean Eng., **31**(17–18), pp. 2175–2208.

[24] Gupta, A., and Tai, W.-C., 2021, "Vibration Suppression of a Harmonically Forced Oscillator Via a Parametrically Excited Centrifugal Pendulum," International Design Engineering Technical Conferences and Computers and Information in Engineering Conference, Online, Virtual, Aug. 17–19, p. V010T10A016.

[25] Gupta, A., Kiet Duong, V. T., and Tai, W.-C., 2023, "Nonlinear Energy Transfer of a Spar-Floater System Using the Inerter Pendulum Vibration Absorber," ASME J. Vib. Acoust., **145**(5), p. 051005.

[26] Gupta, A., and Tai, W.-C., 2024, "Nonlinear Dynamics of a Heaving Spar-Floater System Integrated With Inerter Pendulum Vibration Absorber Power Take-Off for Wave Energy Conversion," Mech. Syst. Signal Process., **209**, p. 111088.

[27] Li, G., and Zhang, S., 2021, "The Hydrodynamic Coefficient Analysis and Motion Control of the Lingyun Moveable Lander," Geofluids, **2021**, pp. 1–23.

[28] Gupta, A., and Tai, W.-C., 2023, "Ocean Wave Energy Conversion With a Spar-Floater System Using a Nonlinear Inerter Pendulum Vibration Absorber," International Design Engineering Technical Conferences and Computers and Information in Engineering Conference, Boston, MA, Aug. 20–23.

[29] Beatty, S. J., Hall, M., Buckham, B. J., Wild, P., and Bocking, B., 2015, "Experimental and Numerical Comparisons of Self-Reacting Point Absorber Wave Energy Converters in Regular Waves," Ocean Eng., **104**, pp. 370–386.

[30] Gupta, A., and Tai, W.-C., 2022, "The Response of an Inerter-Based Dynamic Vibration Absorber With a Parametrically Excited Centrifugal Pendulum," ASME J. Vib. Acoust., **144**(4), p. 041011.

[31] Chakrabarti, S., 2005, *Handbook of Offshore Engineering (2-Volume Set)*, Vol. 1, Elsevier, Amsterdam, The Netherlands.

[32] Heller, V., 2011, "Scale Effects in Physical Hydraulic Engineering Models," J. Hydraul. Res., **49**(3), pp. 293–306.

[33] Rao, M. J., Nallayarasu, S., and Bhattacharyya, S., 2021, "Numerical and Experimental Studies of Heave Damping and Added Mass of Spar With Heave Plates Using Forced Oscillation," Appl. Ocean Res., **111**, p. 102667.

[34] Chen, L.-Q., and Jiang, W.-A., 2015, "Internal Resonance Energy Harvesting," ASME J. Appl. Mech., **82**(3), p. 031004.

[35] Bureau of Safety and Environmental Enforcement, 2024, "Platform Structures Data," https://www.data.bsee.gov/Platform/PlatformStructures/Default.aspx, Accessed November 28, 2024.

[36] Marine Hydrodynamics Laboratory, 2024, "Academics," University of Michigan, Ann Arbor, MI, https://mhl.engin.umich.edu/academics/, Accessed October 10, 2024.
[37] Veritas, N., 2000, *Environmental Conditions and Environmental Loads*, Det Norske Veritas Oslo, Norway.
[38] Mérigaud, A., 2018, "A Harmonic Balance Framework for the Numerical Simulation of Non-Linear Wave Energy Converter Models in Random Seas," Ph.D. thesis, National University of Ireland, Maynooth, Ireland.
[39] Freund, I., 1994, "Optical Vortices in Gaussian Random Wave Fields: Statistical Probability Densities," JOSA A, **11**(5), pp. 1644–1652.
[40] Akbari, H., Panahi, R., and Amani, L., 2020, "Improvement of Double-Peaked Spectra: Revisiting the Combination of the Gaussian and the JONSWAP Models," Ocean Eng., **198**, p. 106965.
[41] Zheng, C.-W., Li, X.-H., Azorin-Molina, C., Li, C.-Y., Wang, Q., Xiao, Z.-N., Yang, S.-B., Chen, X., and Zhan, C., 2022, "Global Trends in Oceanic Wind Speed, Wind-Sea, Swell, and Mixed Wave Heights," Appl. Energy, **321**, p. 119327.
[42] Chen, J., Liu, Z., Song, Y., Peng, Y., and Li, J., 2022, "Experimental Study on Dynamic Responses of a Spar-Type Floating Offshore Wind Turbine," Renew. Energy, **196**, pp. 560–578.
[43] Tuah, H., and Hudspeth, R. T., 1982, "Comparisons of Numerical Random Sea Simulations," J. Waterw. Port Coast. Ocean Division, **108**(4), pp. 569–584.
[44] Cummins, W., 1962, "The Impulse Response Function and Ship Motion," Report 1661, Department of the Navy, David W. Taylor Model Basin, Hydromechanics Laboratory, Research and Development Report.
[45] Ogilvie, T. F., 1964, "Recent Progress Toward the Understanding and Prediction of Ship Motions," Proceedings of the 5th Symposium on Naval Hydrodynamics, Bergen, Norway, Sept. 10–12, pp. 3–80.
[46] Kristiansen, E., Hjulstad, Å., and Egeland, O., 2005, "State-Space Representation of Radiation Forces in Time-Domain Vessel Models," Ocean Eng., **32**(17–18), pp. 2195–2216.
[47] Kristiansen, E., and Egeland, O., 2003, "Frequency-Dependent Added Mass in Models for Controller Design for Wave Motion Damping," IFAC Proc. Vol., **36**(21), pp. 67–72.
[48] Lewandowski, E. M., 2008, "Multi-Vessel Seakeeping Computations With Linear Potential Theory," Ocean Eng., **35**(11–12), pp. 1121–1131.
[49] Newman, J. N., 1977, "The Motions of a Floating Slender Torus," J. Fluid Mech., **83**(4), pp. 721–735.
[50] Warminski, J., and Kecik, K., 2009, "Instabilities in the Main Parametric Resonance Area of a Mechanical System With a Pendulum," J. Sound Vib., **322**(3), pp. 612–628.
[51] Xie, L., Baguet, S., Prabel, B., and Dufour, R., 2017, "Bifurcation Tracking by Harmonic Balance Method for Performance Tuning of Nonlinear Dynamical Systems," Mech. Syst. Signal Process., **88**, pp. 445–461.
[52] Tay, Z. Y., and Venugopal, V., 2019, "The Impact of Energy Extraction of Wave Energy Converter Arrays on Wave Climate Under Multi-directional Seas," J. Ocean Eng. Mar. Energy, **5**, pp. 51–72.
[53] Ulazia, A., Penalba, M., Ibarra-Berastegui, G., Ringwood, J., and Sáenz, J., 2019, "Reduction of the Capture Width of Wave Energy Converters Due to Long-Term Seasonal Wave Energy Trends," Renew. Sustain. Energy Rev., **113**, p. 109267.
[54] Tay, Z. Y., 2019, "Energy Extraction From an Articulated Plate Anti-motion Device of a Very Large Floating Structure Under Irregular Waves," Renew. Energy, **130**, pp. 206–222.
[55] Guillou, N., 2020, "Estimating Wave Energy Flux From Significant Wave Height and Peak Period," Renew. Energy, **155**, pp. 1383–1393.